Robust Optimization Design of High-Frequency Transformer Considering the Effects of Core Cutting

Peng Su¹, Jing Wu¹, Yongjian Li^{1*}, Zhigang Zhao¹, Lujia Xie², and Jiamu Liu¹

¹State Key Laboratory of Intelligent Power Distribution Equipment and System, Hebei University of Technology, Tianjin 300401, China ²School of Electronic Information and Automation, Civil Aviation University of China, Tianjin 300000, China

(Received 15 July 2025, Received in final form 3 September 2025, Accepted 4 September 2025)

The integration of soft magnetic tapes enables the miniaturization, high-efficiency, and high-frequency operation of high-frequency transformers (HFTs), thereby meeting the demands of modern electrical applications. However, the core cutting process can cause localized damage to the tape along the cross-sectional area, resulting in a decrease in magnetic permeability and an increase in core losses near the edges. Consequently, the presence of core cutting introduces numerous unavoidable uncertainties, such as parameter variations, that can affect the performance of HFTs. In response to these challenges, this paper presents a robust optimization design method for HFTs. This method incorporates the manufacturing errors introduced during the core cutting process into the transformer design optimization. This approach accurately predicts the optimization objective uncertainty due to edge degradation, thereby enhancing the reliability of HFTs.

Keywords: core cutting, edge degradation, robust optimization, multi-objective optimization, high-frequency transformer

1. Introduction

Solid-state transformers (SSTs) play a pivotal role in grid regulation, enhancement of power quality, and integration of renewable energy sources. Compared to conventional low-frequency transformers (LFTs), HFTs offer the potential for miniaturization and increased efficiency due to their lighter weight, more compact size, and higher power density [1-3].

Optimized design of HFTs is a necessary step in order to obtain the best performance. Elements typically involved in the optimal design of HFTs are factors such as efficiency, power density, leakage inductance, and temperature, among others. These objectives often exhibit interdependencies and trade-offs, necessitating a holistic approach that accounts for their collective impact [4, 5]. In order to achieve the optimization of HFTs, a novel matrix core structure without increasing the volume is proposed in [2] to improve the thermal performance of the transformer, and efficiency, power density and leakage inductance deviation are used as optimization targets to

fabricate a 50 kVA/20 kHz transformer, which now achieves an efficiency of up to 99.76% and a power density of 24 kW/L. In [6], a 166 kW/20 kHz watercooled nanocrystalline transformer prototype was designed with the goal of maximizing power density and efficiency by introducing a gap to improve losses and thermal behaviour while meeting material constraints and external size limitations, achieving 99.4% efficiency and 44 kW/L power density. An optimal design method based on flux density optimization, aiming to minimize total losses and meet design constraints, was proposed in [7] to design and fabricate a 35 kW/1 kHz silicon steel core mediumfrequency transformer (MFT) prototype. However, the above multi-objective design method for transformers is a deterministic optimization method that does not take into account the uncertainty of manufacturing.

During the manufacturing process of transformer cores, cutting operations introduce plastic deformation and residual stresses, which degrade the magnetic properties of the material near the cut edges and increase losses near the cut surfaces. By establishing a continuous material model, the relationship between local permeability and the distance from the cut edge can be described [8, 9]. Assuming that the mechanical stresses caused by the stamping process decay exponentially from the stamped

©The Korean Magnetics Society. All rights reserved.

*Corresponding author: Tel:

Fax:, e-mail: liyongjian@hebut.edu.cn

edge, the impact of degradation on the B-H characteristics is evaluated from the perspective of mechanical stress. Based on this, the influence of local magnetic field degradation is considered in topological optimization [10]. It is evident that when cores enter mass production, edge degradation caused by cutting can lead to a decline in transformer performances. In [11], the cutting degradation of electrical steel plates is simulated by recalculating the quadrature weights and coordinates, and is applied in actual transformers. Attention has been drawn to how to design and optimize transformers to resist the uncertainty of degraded areas.

To account for the uncertain effects of material and manufacturing errors, robust optimization design methods can be employed to enhance the reliability of machine designs. This method optimizes the machine performance with both the mean and standard deviation of the machine's performance as the design objective, which improves the level of reliability and quality [12, 13]. In [14], an uncertainty characterization method is proposed based on Kriging model, but the uncertainty characterization results are based on a small number of prototypes, which increases the complexity of optimization. In [15], an improved Kriging model with managed uncertainty is proposed to obtain optimal solutions that satisfy different design constraints.

However, in the current core edge degradation research process, the comprehensive consideration of loss, leakage inductance, and other properties is lacking, and the uncertainty caused by cutting is not applied to the optimization design process of the transformer. For this reason, this paper proposes a robust optimization method for HFTs that considers core cutting. To better elaborate on the optimization method, the U-core shell-type transformer is used as an example for the optimization design. In Section 2, the electromagnetic field of HFT is analyzed and the effect of edge degradation on parameters such as loss and leakage inductance is investigated. In Section 3, a detailed robust optimization design strategy is given, which describes in detail how to consider the uncertainty and the robust optimization process. The determination of design variables and optimization objectives, the construction of surrogate models, and the performance evaluation of the optimization results are then presented to demonstrate the effectiveness and accuracy of robust optimization. In Section 4, the HFT prototype is manufactured based on the optimization results for no-load experiments, AC resistance and leakage inductance measurements, and temperature rise measurements to further validate the proposed strategy.

2. Core Cutting Edge Degradation Effect on Electromagnetic Characteristics

Considering the effect of edge degradation caused by core cutting on the electromagnetic characteristics of HFTs plays an important role in improving the performance and reliability of transformers. By studying the effect of edge degradation in depth, a scientific basis for the design and optimization of HFTs can be provided. Consequently, this paper incorporates edge degradation analysis into the design framework and systematically analyzes core loss, AC copper loss and leakage inductance.

2.1. Core Loss Analysis

Core loss is an important part of the total loss of a HFT, and the center cut of the core leads to edge degradation, which affects the core loss. Cut cores exhibit higher core losses compared to uncut cores [16]. The schematic diagram of core loss density as affected by cutting is shown in Fig. 1.

When the input is a non-sinusoidal waveform, the estimation of the iron loss density is usually performed using the modified generalised Steinmetz equation IGSE [17] in order to improve the computational accuracy.

$$P_{c} = \frac{1}{T} \int_{0}^{T} k_{i} \left| \frac{\mathrm{d}B(t)}{\mathrm{d}t} \right|^{\alpha} (\Delta B)^{\beta - \alpha} \, \mathrm{d}t \tag{1}$$

$$k_i = \frac{K}{(2\pi)^{\alpha-1} \int_0^{2\pi} |\cos(\theta)|^{\alpha} 2^{\beta-\alpha} d\theta}$$
 (2)

where K, α , and β are the Steinmetz coefficients, ΔB is the peak-to-peak value of the flux density waveform during one magnetization cycle, and dB(t)/dt is the rate of change of flux density.

In order to reduce the extra cost due to the complex integration function, a square wave with variable duty cycle for HFTs is proposed in [5], and the IGSE can be simplified as:

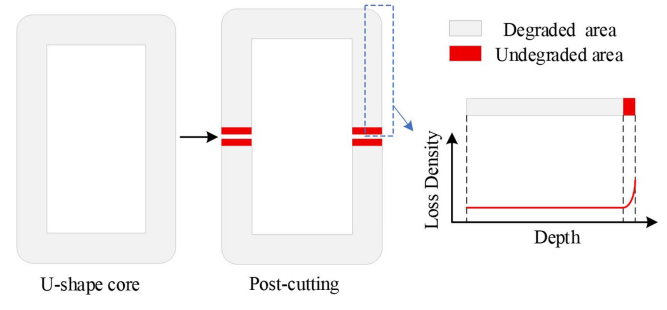


Fig. 1. (Color online) Schematic diagram of core loss density.

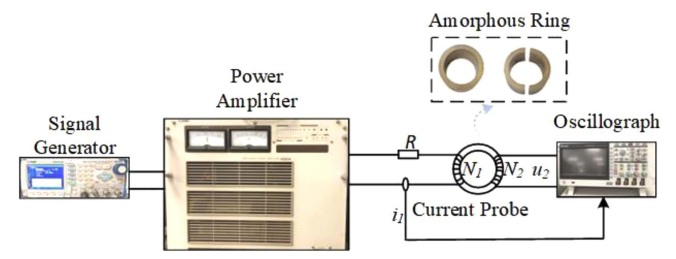


Fig. 2. (Color online) Measurement platform for magnetic ring loss data.

Table 1. Empirical coefficients for IGSE.

	α	β	K
Magnetic core	1.2759	1.6707	1.5536×10 ⁻³
Cutting magnetic core	1.3185	1.6477	1.0879×10 ⁻³

$$P_{c} = 2^{\alpha+\beta} k_{i} f^{\alpha} B_{m}^{\beta} D^{1-\alpha}$$

$$\tag{3}$$

where f is the frequency, B_m is the peak flux density, and D is the duty cycle.

In this paper, a measurement platform for the loss data of magnetic rings is constructed, and measurements are made for both cutting and non-cutting magnetic rings, as shown in Fig. 2. The empirical coefficients of the IGSE are fitted to the loss data of the two types of rings under sinusoidal excitation as shown in Table 1, which shows that the edge degradation and air gap generated by the cutting of the rings lead to the change of the fitted value of the empirical equations. The loss data of the amorphous ring at different frequencies are shown in Fig. 3(a), and the hysteresis line at the magnetization frequency and peak flux density B_m of 10 kHz and 0.4 T, respectively, are shown in Fig. 3(b), and the loss density of the amorphous alloy core is changed from 43.51 W/kg to 46.38 W/kg. Cutting magnetic ring increases the loss density by 6.60% compared to the magnetic ring.

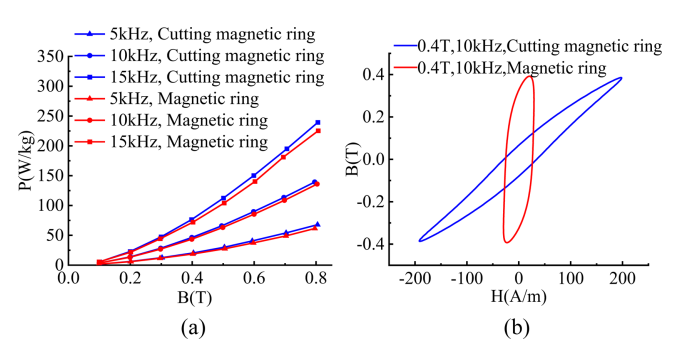


Fig. 3. (Color online) Magnetic ring loss data. (a) Loss data for amorphous magnetic rings at different frequencies; (b) Hysteresis curve.

Therefore, the consideration of the edge degradation of the HFT is of great importance in the optimization of the design.

2.2. AC Copper Loss Analysis

Accurate calculation of AC copper losses is crucial for the design and performance optimization of HFTs. The calculation of AC copper losses is based on Dowell's onedimensional electromagnetic field theory [18], which takes into account the skin effect and proximity effect of alternating current in the conductor to rapidly and accurately calculate the AC copper losses under high-frequency conditions.

Under non-sinusoidal excitation, the high-frequency AC copper losses can be expressed as [19]:

$$P_{winding} = \sum_{n=1}^{N} F_{r,n} R_{\rm dc} I_{\rm rms,n}^2 \tag{4}$$

where $F_{r,n}$ denotes the AC resistance coefficient of the winding, $I_{rms,n}$ represents the root mean square (RMS) value of the n-th harmonic current, and R_{dc} is the direct current (DC) resistance of the winding.

HFTs often employ round Litz wire windings to reduce AC copper losses. The equivalent calculation process of the Litz wire winding, through step-by-step area equivalence, is illustrated in the Fig. 4. To ensure that the conductor generates an equivalent magnetic field strength before and after the equivalence, a porosity factor is introduced to correct the electrical conductivity of the conductor [20, 21]. The correction factor is given by the equation:

$$\begin{cases}
\sigma_{w}' = \sigma_{w} \eta \\
\eta = \frac{\sqrt{\pi N_{s}} d_{s}}{2(D_{L} + d_{L})} \frac{h_{w}}{h_{c}}
\end{cases} \tag{5}$$

where N_s is the number of individual fine wires contained in each Litz wire bundle, D_L is the outer diameter of the

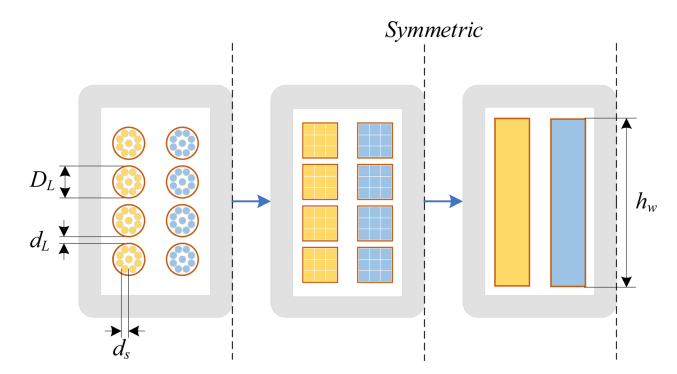


Fig. 4. (Color online) The equivalent process of Litz wire winding.

Litz wire bundle, d_s is the diameter of the individual fine wire, d_L is the distance between Litz wire bundles, h_w is the height of the equivalent copper foil winding, and h_c is the height of the core window.

The AC resistance coefficient of the winding is:

$$F_r = \Delta [\xi_1 + \frac{2}{3}(m^2 N_s - 1)\xi_2]$$
 (6)

where *m* represents the number of winding layers, Δ is the winding penetration factor, $\xi_1 ? \xi_2$ are the skin effect correction factor and proximity effect correction factor of the winding, respectively.

$$\begin{cases} \xi_{1} = \frac{\sinh(2\Delta) + \sin(2\Delta)}{\cosh(2\Delta) - \cos(2\Delta)} \\ \xi_{2} = \frac{\sinh\Delta - \sin\Delta}{\cosh\Delta + \cos\Delta} \end{cases}$$
 (7)

$$\Delta = \sqrt{n} \frac{d_s}{2\delta_{\cdots}} \sqrt{\pi \eta} \tag{8}$$

where δ_w is the skin depth and the expression:

$$\delta_{w} = \sqrt{\frac{1}{\sigma_{w}^{'} \pi f \mu_{0}}} \tag{9}$$

Equations (4) to (9) accurately characterize the skin effect and proximity effect of the Litz wire, and are applicable for calculating the AC copper losses of HFTs with a layered winding structure using circular Litz wire as the conductor. In actual selection, to effectively control high-frequency losses, d_s/δ_w needs to be controlled within a reasonable range. To investigate the effect of skin depth on AC copper losses, the F_r was calculated under different d_s/δ_w conditions, with the m varying from 1 to 3. The curve of F_r versus d_s/δ_w is shown in Fig. 5. As can be seen from Fig. 5, the higher the number of layers, the

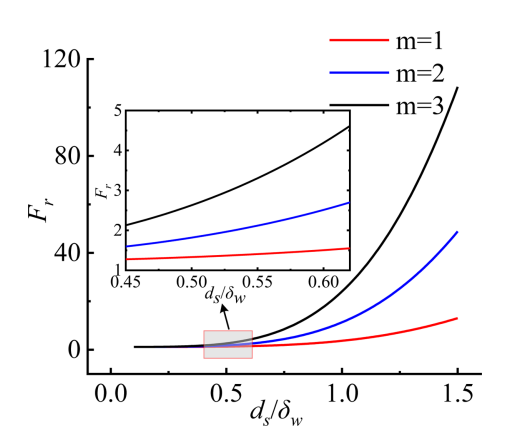


Fig. 5. (Color online) F_r variation relationship with d_s/δ_w

more significant the high-frequency effect of the winding. As d_s/δ_w increases, the skin effect and proximity effect in the winding become increasingly significant, resulting in an increasingly larger F_r value.

When the core is cutting from the center resulting in edge degradation, the symmetry of its magnetic circuit structure will be destroyed, which leads to significant changes in the leakage field and current density and affects the AC copper losses. To verify the effect of cutting on AC copper losses, an air gap of 25 µm is set along the symmetrical region in the middle of the cut core, and degradation regions with a degradation depth of 0.1 mm are set along both sides of the air gap in the middle. Taking the transformer structure in Fig. 6(a) as an example, the computed AC resistance coefficients are shown in Fig. 6(b). The F_r of amorphous cutting core and amorphous core roughly increase with increasing frequency. At 200 kHz, the F_r of the amorphous cutting core is 1.11 times that of the amorphous core, demonstrating the pronounced impact of edge degradation.

To further verify the effect of cutting on the core AC

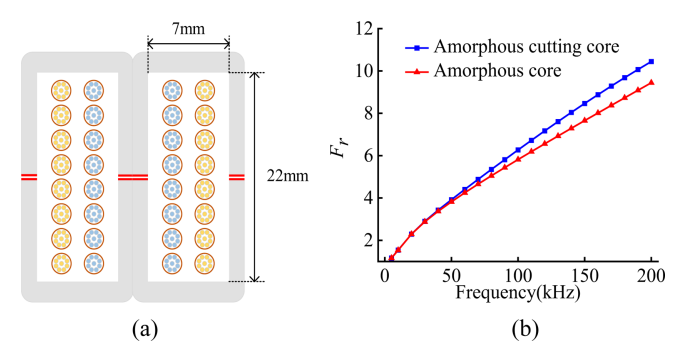


Fig. 6. (Color online) Transformer structure and AC resistance coefficient. (a) Transformer 2D structure; (b) AC resistance coefficients.

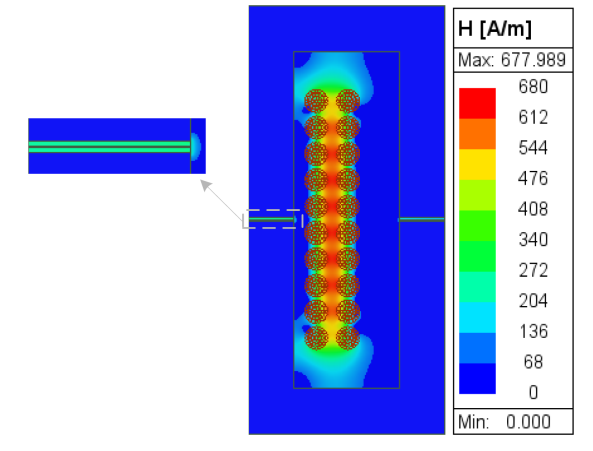


Fig. 7. (Color online) Cloud plot of leakage field strength.

copper losses, Fig. 7 gives the electromagnetic field characteristics inside the window of an HFT core with edge degradation effect under a 1A current excitation at 10 kHz and shows that the magnetic field near the cutting edge is significantly distorted due to permeability degradation. Simulation studies show that cutting the air gap and the degraded region leads to a significant increase in the local magnetic field strength, and the inhomogeneous distribution of the leakage field generates high-frequency eddy currents in the windings, which in turn cause additional losses.

2.3. Leakage inductance

In HFTs, due to the incomplete coupling of the primary and secondary winding fluxes, there will be some leakage flux present, which leads to the formation of leakage inductance [22]. For the calculation of leakage inductance, the effect of core material on leakage inductance is considered by magnetic-image method in [23, 24], and the leakage inductance is obtained by finite element electromagnetic field analysis for a given transformer geometry in [25]. The leakage inductance of the transformer can be calculated by combining the relationship between leakage energy and leakage inductance, as shown in equation (10).

$$W_{\sigma} = \frac{1}{2} L_{\sigma} I_{rms}^{2} = \frac{1}{2} \mu \int_{V} H^{2} dV$$
 (10)

where H is the magnetic field strength in the desired range, μ is the magnetic permeability in the desired range, and V is the volume of the desired range.

Taking the transformer structure shown in Fig. 6(a) as an example, different degradation depths ranging from 0 mm to 1 mm are applied at various frequencies. The leakage inductance is calculated using finite element analysis (FEA), and the results are presented in Fig. 8. It

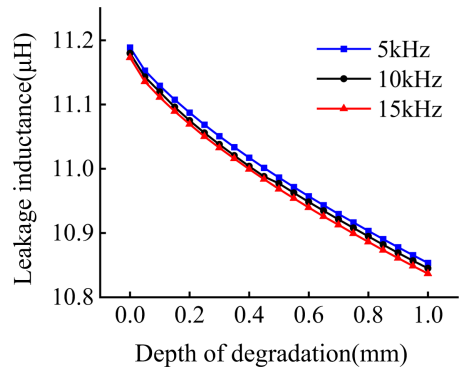


Fig. 8. (Color online) Variation of leakage inductance for different frequencies and degradation depths.

can be observed that the leakage inductance decreases with increasing degradation depth. For example, when the frequency is 10 kHz and the degradation depth is 1mm, the leakage inductance decreases by 3.0%, so it is necessary to consider the influence of edge degradation on the optimal design of HFT.

3. Optimizing Strategy Considering Edge Degradation Effect

U-core cut cross section shown in Fig. 9, along the core cut cross section will cause edge degradation, assuming that the degradation region of the U-core shell-type transformer is divided into four parts as shown in Fig. 10(a), the depth of the four regions, D_i (i = 1, 2, 3 and 4) follow a normal distribution shown in equation (11), and Fig. 10(b) shows the relationship between the sigma grade and the normal distribution. According to the three-sigma principle, the edge degradation of the transformer rate will fall within an acceptable rang with within ± 3 standard deviations of the mean value.

$$D_{i} \sim N\left(0.1, \left(\frac{1}{30}\right)^{2}\right) \quad (i = 1, 2, 3, 4)$$
 (11)

According to probability theory, the probability density function of the deterioration region of the HFT can be expressed by the following equation.

$$f(D_{i}) = \frac{1}{\sqrt{2\pi\sigma}} e^{-\frac{(D_{i}-\mu)^{2}}{2\sigma^{2}}}$$
 (12)

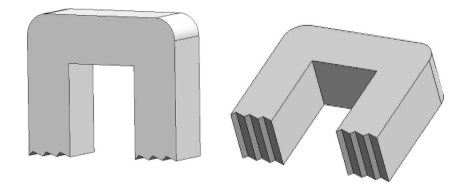


Fig. 9. U-core cut cross section.

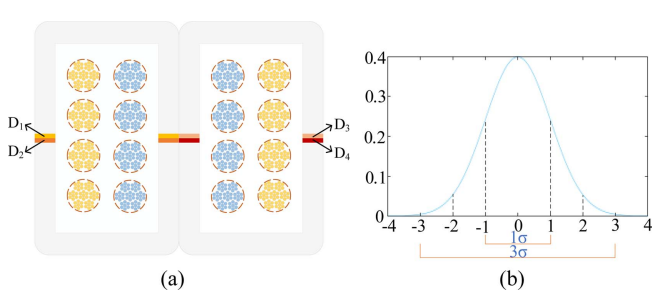


Fig. 10. (Color online) HFT considering edge degradation. (a) The four parts of edge degradation; (b) Relationship between sigma grade and standard normal distribution.

where μ and σ are the mathematical expectation and standard deviation.

To consider the uncertainty of the core cutting process during optimization, Fig. 11 shows the flowchart of the robust optimization design strategy. Firstly, a sensitivity analysis is performed according to the basic performance index of the transformer to determine the key parameters affecting its performance and determine the range of values for these parameters for the design of experiments (DOE). Next, the Optimized Latin Hypercube Method (OLHS) is used to sample different sizes of the transformer experimentally. To account for uncertainty introduced by the machining process, a normal distribution is introduced to simulate edge degradation of the core. Various edge degradation situations that may occur during production are simulated for a specific combination of structural parameters. The Kriging model is developed by FEA simulation of the HFTs model for calculating the mean and standard deviation of transformer losses, relative error of leakage inductance and volume size. This model is then used to construct the robust optimization objective. The response surface model (RSM) is constructed based on the experimental data and is used to predict transformer performances under different parameter combinations. Then, the Pareto front is obtained using the Non-dominated Sorting Genetic Algorithm-II (NSGA-II).

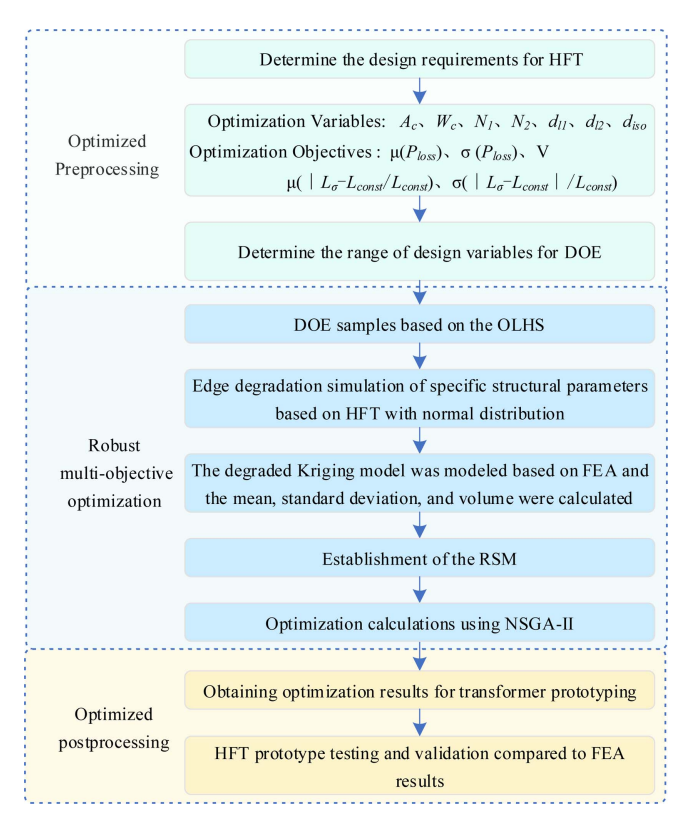


Fig. 11. (Color online) Optimization flowchart of HFT.

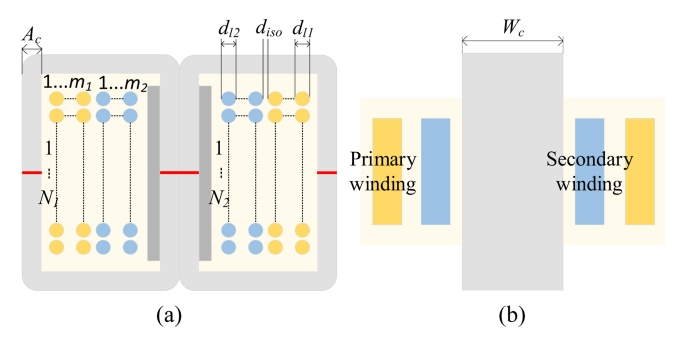


Fig. 12. (Color online) Parameter model of the HFT. (a) Front view of the HFT; (b) Side view of the HFT.

Table 2. HFT design requirements.

Parameter	Symbol	Value
Power	P	10 kVA
Operation frequency	f	10 kHz
Voltage	$V_{p,s}$	400/400 V
Ratio	n	1

Finally, a transformer prototype is manufactured based on the optimization results, which are verified by simulation analysis and experimental tests.

During the optimization process of the HFT design, the structural dimensions of the transformer are parameterised based on the preliminary calculation parameters outlined in Table 2. The established structural design scheme for the HFT is presented in Fig. 12.

Due to the large number of design parameters, this can increase computational costs and reduce computational efficiency. Therefore, this paper employs sensitivity analysis to identify decision variables that significantly impact the design outcome. This approach allows for a comprehensive assessment of the impact of each variable on the optimization objectives, selecting structural factors with higher sensitivity as optimization variables. This paper ultimately selects the following design variables: the core cross section side length A_c ; the width W_c of the core tape; the number of turns per layer in the primary winding N_1 (equal to that in the secondary winding N_2); the primary winding wire diameter d_{l2}); and the insulation spacing d_{lso} between the primary and secondary windings.

After obtaining the initial design requirements, it is necessary to further determine the objective functions and constraints to construct a surrogate model. In the design process of HFTs, reducing losses and volume are key objectives, while leakage inductance must also meet the operational requirements of HFTs. Therefore the optimization objective selected in this paper is set as:

Functions:
$$\begin{cases} \min P_{loss} = P_{core} + P_{windings} \\ \min \frac{\left| L_{\sigma} - L_{const} \right|}{L_{const}} \\ \min V = V_{core} + V_{windings} \end{cases}$$
 (13)

In Dual Active Bridge (DAB) converter, the leakage inductance is used to realize energy transfer and soft switching the leakage inductance needs to meet the power transfer demand, in this paper, the HFT leakage inductance setting value is L_{const} . At the same time, to ensure that the DAB converter can achieve zero-voltage switching, the leakage inductance should be greater than the minimum leakage inductance value $L_{\sigma-min}$ required for isolation. To avoid core saturation, the maximum magnetic flux density B_m should be less than the saturation magnetic flux density B_{sat} of the material. Additionally, in this paper, certain safety margins are introduced to avoid the risk of damage due to magnetic saturation and to cope with the effects of temperature variations. Thus, the inequality constraints selected for this paper are set as follows:

$$s.t.: \begin{cases} x_1 \le x \le x_u \\ L_{\sigma} \ge L_{\sigma-\min} \\ B_m \le (1 - k_{saf}) * B_{sat} \end{cases}$$
 (14)

where x_l is the lower limit of the decision variable, x_u is the upper limit of the decision variable, k_{saf} is the safety margin, and the safety margin of 25% is selected in this paper.

To ensure that the voltage ratio is strictly 1:1 and to avoid voltage deviation or magnetic flux imbalance caused by differences in the number of turns, the number of turns in the primary and secondary windings is equal. In addition, electromagnetic symmetry is improved by making the outer diameters of the primary and secondary windings equal. Therefore, the equation constraints in this paper are as follows:

$$s.t.:\begin{cases} N_p = N_s \\ d_{l1} = d_{l2} \end{cases}$$
 (15)

In order to consider the uncertainty factors in the core cutting process, the traditional deterministic optimization model is transformed into a robust optimization model, assuming that the deterioration depth caused by core cutting all obey normal distribution, so the optimization objectives and constraints of the robust optimization model are as follows:

Functions:
$$\begin{cases} \min \mu(P_{loss} = P_{core} + P_{windings}) \\ \min \sigma(P_{loss} = P_{core} + P_{windings}) \\ \min \mu(\frac{\left|L_{\sigma} - L_{const}\right|}{L_{const}}) \\ \min \sigma(\frac{\left|L_{\sigma} - L_{const}\right|}{L_{const}}) \\ \min V = V_{core} + V_{windings} \end{cases}$$
(16)

$$\begin{cases} x_{1} \leq x \leq x_{u} \\ L_{\sigma} \geq L_{\sigma-\min} \\ B_{m} \leq (1 - k_{saf}) * B_{sat} \end{cases}$$

$$s.t.: \begin{cases} N_{p} = N_{s} \\ d_{l1} = d_{l2} \end{cases}$$

$$D_{i} \sim N \left(0.1, (\frac{1}{30})^{2} \right) \quad (i = 1, 2, 3, 4)$$

The reduction of the computational burden can be achieved through the construction of a surrogate model. Initially, the sampling of different sizes of the structure of the HFT was accomplished through OLHS, and then the distribution of the edge degradation was simulated based on the normal distribution, and the computation of the transformer optimization objective function was accomplished through the Kriging model. Then the RSM is built

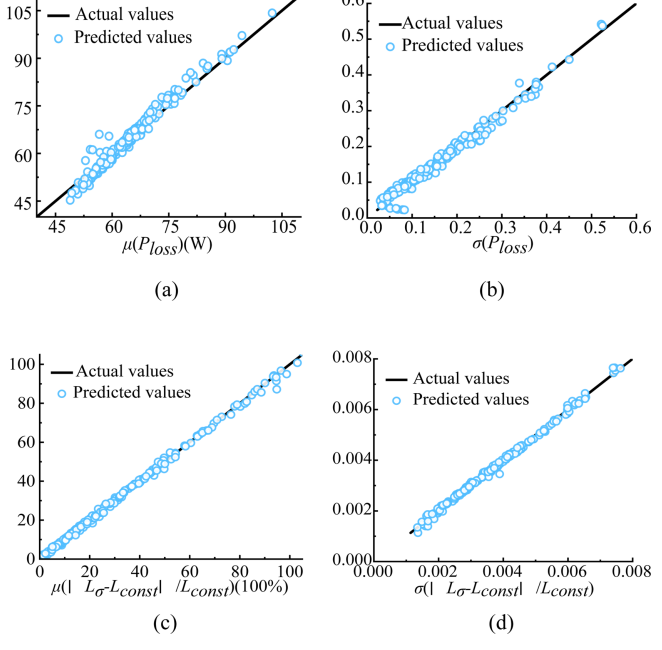


Fig. 13. (Color online) Validation results of RSM. (a) $\mu(P_{loss})$; (b) $\sigma(P_{loss})$; (c) $\mu(|L_{\sigma}-L_{const}|/L_{const})$; (d) $\sigma(|L_{\sigma}-L_{const}|/L_{const})$.

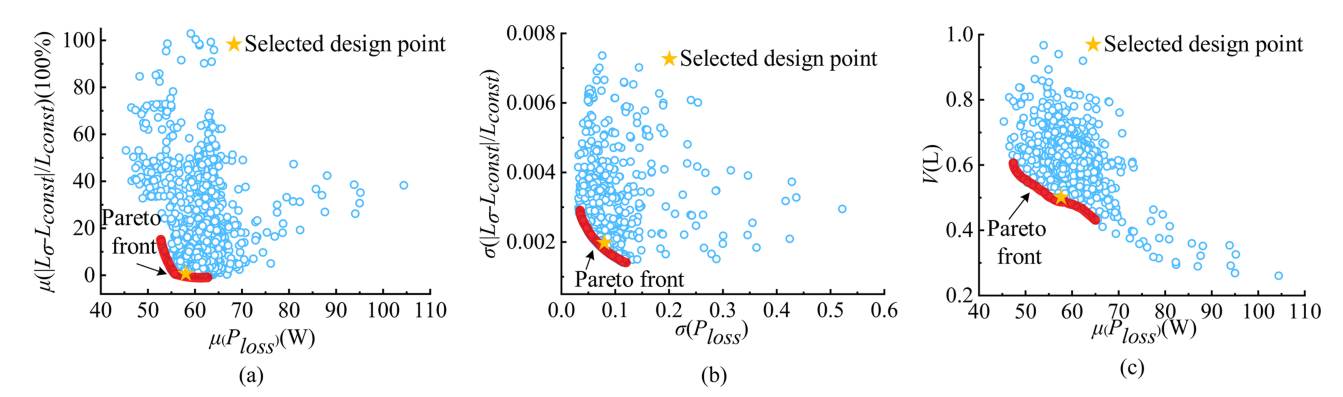


Fig. 14. (Color online) Distribution of the five optimization variables. (a) Plot of mean distribution; (b) Plot of standard deviation distribution; (c) Plot of loss mean and volume.

based on the inputs and outputs of the sample points. Finally, to assess the accuracy of the RSM, the actual and predicted values of the model are compared to verify the accuracy and reasonableness of the model as shown in Fig. 13.

The NSGA-II algorithm is extensively utilized in the realm of multi-objective optimization. It incorporates a fast non-dominated sorting mechanism, which effectively guides the search process and provides stable optimization outcomes even when confronted with uncertainties. Within the NSGA-II algorithm, the mean μ , the standard deviation σ , and volume are established as optimization objectives. Each individual within the population is required to compute the corresponding values. Through the application of selection, crossover, and mutation operators, the algorithm ultimately yields the Pareto front optimal design set. To further illustrate the performance distribution of the HFT, Fig. 14 shows the distribution of the five optimization objectives, respectively.

NSGA-II does not preset target weights, comprehensively revealing the complex trade-off between loss characteristics, relative error of leakage inductance, and volume. In the Pareto optimal solution set, we selected the final solution based on a trade-off analysis according to the core design constraints: under the constraints, our goal was to minimize the standard deviation of loss and the standard deviation of leakage inductance relative error, thereby

Table 3. Comparison of optimization results.

Optimization objectives	Initial	Determinism	Robustness
$\mu\left(P_{loss}\right)\left(\mathbf{W}\right)$	64.37	57.99	58.47
$\sigma(P_{loss})$	0.191	0.123	0.086
$\mu(L_{\sigma}\text{-}L_{const} /L_{const}) (100\%)$	14.13	2.01	2.25
$\sigma(L_{\sigma}\text{-}L_{const} /L_{const})$	0.00409	0.00352	0.00214
Power density (kW/L)	19.01	20.16	19.49

reducing the uncertainty of edge degradation caused by HFT core cutting and improving system robustness. Table 3 provides a comparison of the optimization results for the initial design, deterministic optimization, and robust optimization of the HFT.

To further verify the effectiveness of robust optimization, a detailed comparison of the performances of HFTs before and after optimization was conducted. The Fig. 15 shows the normal distribution of losses and relative errors of leakage inductance under three conditions when the same disturbance is applied. Taking losses as an example, as shown in Fig. 15(a), the losses of the HFT are concentrated at 64.37W, 57.99W, and 58.47W, with standard deviations of the normal distribution being 0.191, 0.123, and 0.086, respectively. It can be seen that, compared to the original design, the losses have decreased by 9.91% and 9.17% for deterministic optimization and robust optimization, respectively. However, the standard deviation for robust optimization is smaller than that for deterministic optimization, indicating stronger robustness in losses.

Since the optimization of HFTs also needs to consider the effect of volume, the power density of the three cases

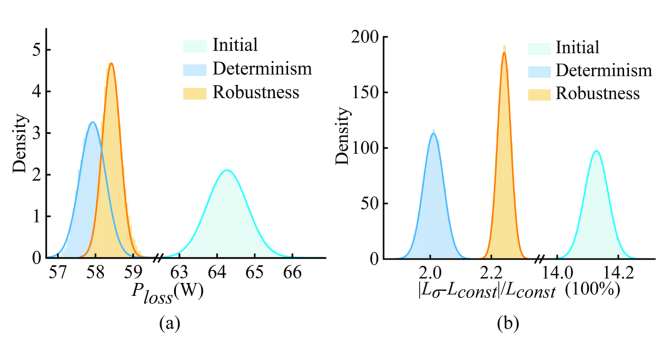


Fig. 15. (Color online) Normal distribution. (a) P_{loss} ; (b) $|L_{\sigma}-L_{const}|/L_{const}$.

is further analyzed and compared. The power density of the initial design is 19.01 kW/L, and different optimizations are carried out for the initial design, and the result of deterministic optimization is 20.16 kW/L, and the result of robust optimization is 19.49 kW/L. The deterministic optimization improves the power density by 6.05% while the robust optimization improves the power density by 2.55%. Although the power density enhancement of deterministic optimization is more significant, its robustness is weaker. Therefore, the application of the HFT structure designed using robust optimization to manufacturing helps to improve its overall performance and reliability.

4. Experimental Verification

In order to minimize the relative error of leakage inductance while achieving efficiency and size, a design scheme such as the one selected in Fig. 14 is chosen, and the key parameters of the selected design are shown in Table 4.

The HFT prototype utilizing the optimal design solution is fabricated with the 3D structure shown in Fig. 16(a) and the HFT prototype shown in Fig. 16(b). For the manufactured HFT prototype, the core is made of amorphous material. To facilitate assembly, the two amorphous magnetic cores are cut into a U-shape using a diamond wire cutting process. However, since the cross-section of the U-core is rough after cutting, there will be a slight air gap during assembly. The winding structure

Table 4. Electrical parameters.

Prameter	Symbol	Value
Core cross section side length	A_c	21.8 mm
Core tape width	W_c	20 mm
Primary winding	$m_1 \times N_1$	2×15
Secondary winding	$m_2 \times N_2$	2×15
Primary/Secondary winding diameter	d_{l1}/d_{l2}	4.3 mm
Insulation spacing	d_{iso}	2 mm

consists of two layers, each layer of 15 turns, round Litz wire strand wire diameter of 0.1 mm, a turn of Litz wire including 1000 strands, a single turn of the Litz wire diameter of 4.3 mm. The outer layer of the core and the interlayer of the winding are wrapped with polyimide film to provide insulation. The skeleton is made of polyamide fiber, which has excellent temperature insulation performance.

During the experiment, the cores were strictly aligned using fixtures to ensure that the air gap size was stably controlled at the process minimum. In the simulation modeling, the air gap value was set to 25 µm. To quantify the independent and coupled effects of the air gap and core degradation, this paper compares the performance of two models at frequencies from 8 kHz to 12 kHz: Model I, which considers the combined effects of the air gap and core degradation, and Model II, which only considers the air gap. The comparison between the two models and the experimental results is shown in the Fig. 17. As shown in Fig. 17(a), the average relative errors of the core loss between Model I and Model II and the measured values are 6.92% and 10.93%, respectively. As shown in Fig. 17(b), the average relative errors of the AC resistance coefficient between Model I and Model II and the measured values are 5.20% and 7.18%, respectively. Therefore, the presence of the air gap affects the performance of the transformer, and the impact of degradation cannot be

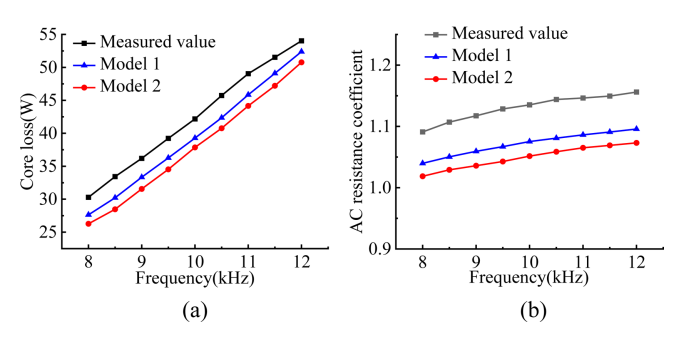


Fig. 17. (Color online) Model comparison. (a) Core loss; (b) AC resistance coefficient.

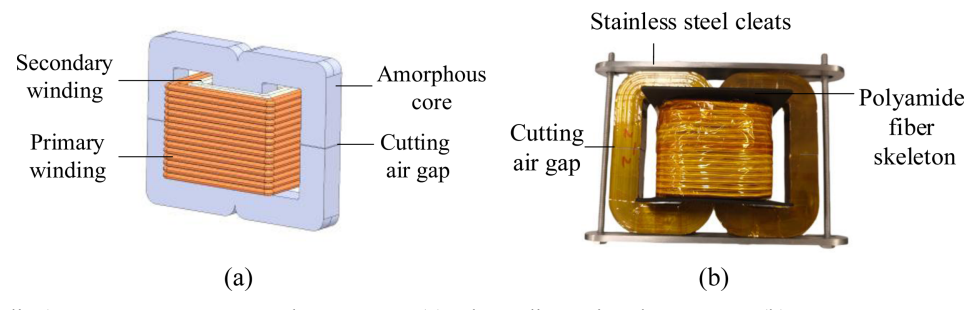


Fig. 16. (Color online) HFT 3D structure and prototype. (a) Three-dimensional structure; (b) Prototype.

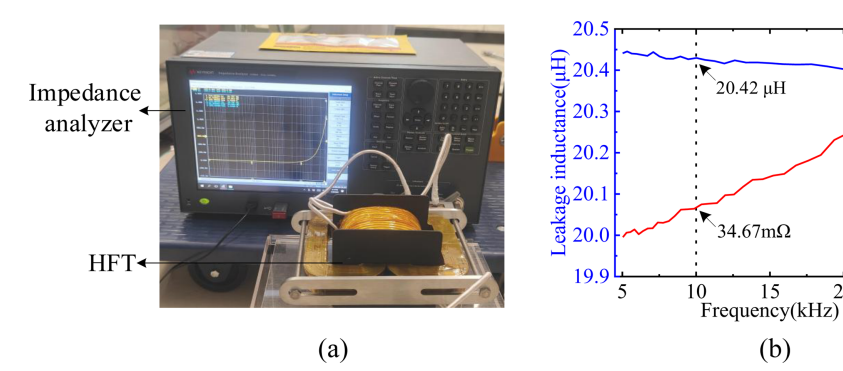


Fig. 18. (Color online) AC resistance and leakage inductance measurement platform. (a) Measurement platform; (b) Measurement results.

ignored. The model that simultaneously considers both the air gap and edge degradation is closer to the actual values.

To measure the leakage inductance and AC resistance values of the HFT prototype, a measurement platform was built as shown in Fig. 18(a). The leakage inductance and AC resistance of the HFT prototype were measured by KEYSIGHT E4990A impedance analyzer. To ensure the accuracy of the measurements, the secondary winding of the HFT prototype was short-circuited. The measurements of AC resistance and leakage inductance of the HFT are shown in Fig. 18(b). The measured result shows that the leakage inductance is 20.42 μ H, and the finite element calculation result is 19.25 μ H. The error between the simulated result and the measured value is 5.72%, which is within the reasonable range. The measured AC

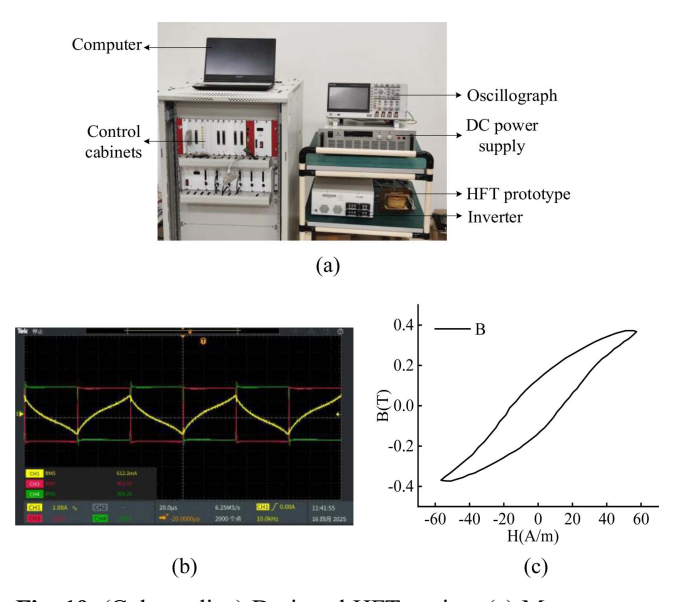


Fig. 19. (Color online) Designed HFT testing. (a) Measurement platform; (b) Measured voltage and current waveforms; (c) Hysteresis curve.

resistance of the winding of the HFT is $34.67~\text{m}\Omega$, and the calculation result is $31.40~\text{m}\Omega$. The error between the simulated result and measured value is at 9.43%. In the actual production process, the skeleton size and insulation distance of the HFT have some differences compared with the design value, in addition, the simulation software can not be completely based on the actual simulation of the Litz wire winding, the magnetic field intensity distribution will be different from the actual situation, resulting in the leakage inductance and winding loss measurements can not be completely consistent with the design value.

50

30

25

A no-load test platform is constructed as shown in Fig. 19(a), and the transformer with a square wave voltage of amplitude 400 V and a frequency of 10 kHz, while the secondary winding is kept open circuit. Measure the primary current and secondary voltage as shown in Fig. 19(b), and obtain the hysteresis curve of the core as shown in Fig. 19(c). The experimental measurement of transformer core loss is 42.18 W, the finite element simulation value is 39.27 W, with an error of 6.90%, and the result calculated by using IGSE is 46.31 W, which is 9.79% higher than the experimentally measured value, and the results are all within a reasonable limit.

To further verify the thermal characteristics of the HFT during stable operation, the simulation is carried out using Icepak simulation software, and the simulation results are shown in Fig. 20(a), with the highest temperature concentrated in the core at 107.7°C. Under the condition of ambient temperature of 25°C, after the transformer runs for 2h, the steady state temperature distribution of the transformer is photographed by FLUKE Ti32 infrared thermal imager, as shown in Fig. 20(b), and the maximum temperature reaches 116.3°C, which is roughly the same as the simulation result and meets the design requirements.

In addition, to verify the robust performance before and after considering the cutting effect, three different amorphous

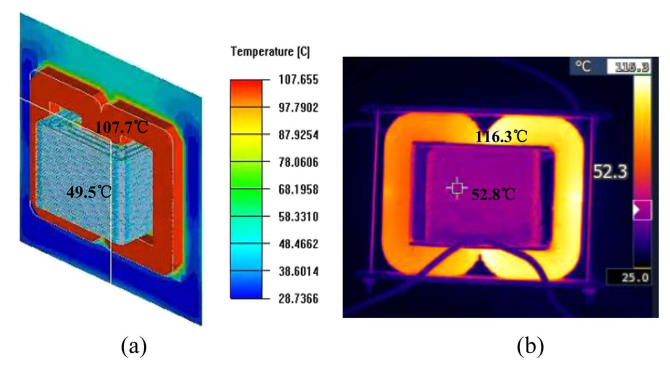


Fig. 20. (Color online) Temperature rise distribution of the transformer. (a) Simulation results; (b) Experimental measurements.

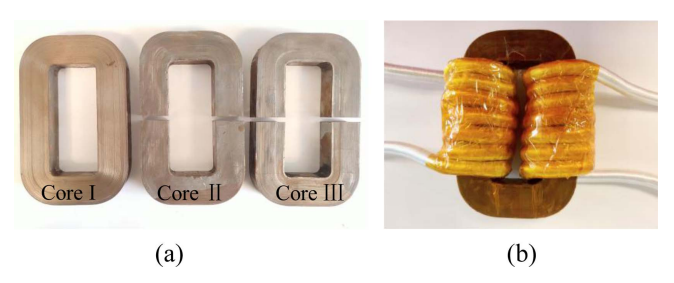


Fig. 21. (Color online) Core and prototype (a) Three sets of amorphous cores; (b) Transformer structure.

cores were used, as shown in Fig. 21(a). Core I is a complete core, while Cores II and III are cores with the same structure as Core I but cut along the central symmetry line using a diamond wire. Cores II and III, which are produced by the same manufacturer, may exhibit certain differences in material properties and air gap processes due to fluctuations in the manufacturing process, resulting in varying degrees of performance deviation. Therefore, this paper compares two cutting cores with a complete core. By comparing cutting cores with the complete core, the influence of cutting as a source of uncertainty was introduced, and the variability in performance caused by the cutting process was quantified.

According to the experimental platform shown in Fig. 18(a), leakage inductance and AC resistance measurements were conducted under identical conditions. All three sets of cores employed the same winding structure, as illustrated in Fig. 21(b). Both the primary and secondary windings were wound with 7 turns using Litz wire with an outer diameter of 9.90 mm, specification 0.1×5000, with a strand diameter of 0.1 mm and 5000 strands per turn of Litz wire. Since the prototype designed in this paper, as shown in Fig. 16, operates at a frequency of 10 kHz, the center frequency is set to 10 kHz here, with a variation range of ±2%. Fig. 22 shows the normal

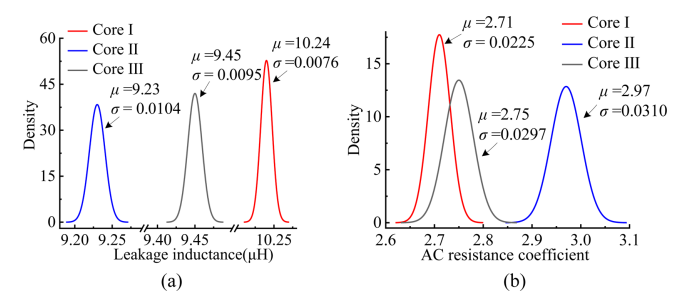


Fig. 22. (Color online) Normal distribution. (a) Leakage inductance; (b) AC resistance coefficient.

distribution of leakage inductance and AC resistance coefficients for the complete core and cutting core under the same conditions. As shown in the Fig. 22(a), taking the leakage inductance distribution as an example, compared to Core I, the mean leakage inductance of Cores II and III decreased by 9.86% and 7.71%, respectively, but the standard deviation increased by 36.84% and 25.05%, respectively. The complete core has inherently high consistency and low fluctuation in performance. However, when considering the effects of degradation, the cutting process itself has a high degree of uncertainty, significantly reducing the robustness of HFTs.

Furthermore, to compare the effect of cutting on transformer core loss, using the experimental platform shown in Fig. 19(a), the same winding was wound on the three cores shown in Fig. 21(a), and a prototype transformer was constructed as shown in Fig. 23(a). The loss amplitude was measured at 10 kHz with a magnetic flux density of 0.4T and a fluctuation of ± 0.01 T, as shown in Fig. 23(b). Core I fluctuated between 14.21 W and 18.20 W, with a mean and standard deviation of 16.21 W and 0.4986, respectively. Core II fluctuated between 25.08 W and 30.61 W, with a mean and standard deviation of 27.85 W and 0.6915, respectively. Core III fluctuates between 23.97 W and 28.77 W, with a mean and standard

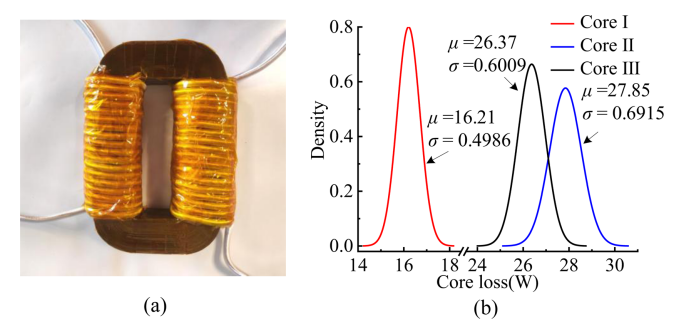


Fig. 23. (Color online) Transformer prototype and normal distribution diagram. (a) Transformer prototype; (b) Normal distribution diagram of core loss.

deviation distribution of 26.37 W and 0.6009, respectively. Therefore, compared to the uncut core, cutting cores exhibit lower robustness and a wider fluctuation range. However, cutting facilitates assembly. Additionally, by studying the impact of edge degradation effects and their uncertainties on performance errors, this research provides direct guidance for optimizing cutting processes and designing transformers.

5. Conclusion

In this paper, a robust HFT optimization strategy considering edge degradation uncertainty is proposed to consider the effects of core cutting on the HFT electromagnetic field distribution and key parameters. The introduction of a normal distribution can reduce the effects of uncertainty on the electromagnetic performance of the HFT compared with traditional deterministic optimization, thus improving the robustness, stability, and reliability of the optimization process. To verify the proposed optimization strategy, a 10 kVA, 10 kHz HFT is designed and manufactured, and the HFT electromagnetic performance is compared with that of the initial design and the deterministic optimization scheme. The efficiency of the HFTs fabricated according to the robust optimization design scheme is as high as 99.36%, with no thermal operation problems, which meets the design requirements.

Acknowledgement

This work was supported by the Continuation Funding Project for Innovative Research Groups of Natural Science Foundation of Hebei Province E2024202298; the Natural Science Foundation of China under Grant 52407072, 52477043 and 52130710; the Natural Science Foundation of Hebei Province under Grant E2024202205; the Fundamental Research Funds for the Central Universities under Grant 3122025PT20 and Multi-Funding Project of the Tianjin Natural Science Foundation 24JCQNJC00160.

References

- [1] Z. Li, E. Hsieh, Q. Li, and F. C. Lee, IEEE Trans. Power Electron. **38**, 9917 (2023).
- [2] Z. Wan, Y. Li, H. Wang, and X. Li, IEEE Trans. Power Electron. **39**, 12384 (2024).

- [3] T. O. Olowu, H. Jafari, M. Moghaddami, and A. I. Sarwat, IEEE Trans. Ind. Appl. 57, 1014 (2021).
- [4] L. Zhang, X. Li, X. Zhu, and C. Zhang, IEEE Trans. Ind. Electron. **72**, 6762 (2025).
- [5] M. Mogorovic and D. Dujic, IEEE Trans. Power Electron. 34, 1696 (2019).
- [6] M. Leibl, G. Ortiz, and J. W. Kolar, IEEE J. Emerg. Sel. Top. Power Electron. 5, 110 (2017).
- [7] P. Huang, C. Mao, D. Wang, L. Wang, Y. Duan, J. Qiu, G. Xu, and H. Cai. IEEE Trans. Ind. Electron. 64, 4391 (2017).
- [8] S. Elfgen, S. Steentjes, S. Böhmer, D. Franck, and K. Hameyer, IEEE Trans. Ind. Appl. **53**, 1978 (2017).
- [9] R. Sundaria, D. G. Nair, A. Lehikoinen, A. Arkkio, and A. Belahcen, IEEE Trans. Ind. Electron. 67, 7354 (2020).
- [10] Y. Hidaka and H. Igarashi, IEEE Trans. Magn. 53, 1 (2017).
- [11] I. T. Gürbüz, F. Martin, P. Rasilo, M. M. Billah, and A. Belahcen, J. Magn. Magn. Mater. **593**, 171843 (2024).
- [12] J. Wu, X. Zhu, D. Fan, Z. Xiang, L. Xu, and L. Quan, IEEE Trans. Magn. **58**, 1 (2022).
- [13] L. Zhang, M. Zhang, X. Zhu, Z. Pei, and X. Chen, IEEE Trans. Ind. Electron. 72, 6865 (2025).
- [14] S. Kim, S.-G. Lee, J.-M. Kim, T. H. Lee, and M.-S. Lim, IEEE Trans. Energy Convers. **35**, 2056 (2020).
- [15] H. Zhang, G. Wang, J. Zhang, Y. Gao, W. Hua, and Y. Wang, IEEE Trans. Ind. Appl. 60, 6799 (2024).
- [16] W. Shen, F. Wang, D. Boroyevich, and C. W. Tipton IV, IEEE Trans. Ind. Appl. 44, 213 (2008).
- [17] K. Venkatachalam, C. R. Sullivan, T. Abdallah, and H. Tacca, 2002 IEEE Workshop Comput. Power Electron. (COMPEL). Mayaguez (2002) pp. 36-41.
- [18] P. L. Dowell, Proc. Inst. Electr. Eng. 113, 1387 (1966).
- [19] A. Arruti, I. Aizpuru, M. Mazuela, Z. Ouyang, and M. A. E. Andersen, IEEE Trans. Power Electron. 39, 16371 (2024).
- [20] Y. Wang, W. Chen, and Z. Shen, IEEE Trans. Power Electron. **39**, 1135 (2024).
- [21] R. P. Wojda and M. K. Kazimierczuk, IEEE Trans. Ind. Appl. 54, 3548 (2018).
- [22] Z. Ouyang, J. Zhang, and W. G. Hurley, IEEE Trans. Power Electron. **30**, 5769 (2015).
- [23] X. Margueron, A. Besri, P.-O. Jeannin, J.-P. Keradec and G. Parent, IEEE Trans. Ind. Appl. 46, 1055 (2010).
- [24] W. A. Roshen, IEEE Trans. Magn. 26, 2880 (1990).
- [25] M. Nazmunnahar, S. Simizu, P. R. Ohodnicki, S. Bhattacharya, and M. E. McHenry, IEEE Trans. Magn. **55**, 1 (2019).